



# Effects of different polymer precursors on the characteristics of SiOC bulk ceramics

Lixia Wang<sup>1,2</sup> · Kathy Lu<sup>2</sup> · Ruixin Ma<sup>3</sup>

Received: 28 January 2019 / Accepted: 1 May 2019 / Published online: 10 May 2019  
© Springer-Verlag GmbH Germany, part of Springer Nature 2019

## Abstract

Silicon oxycarbide (SiOC) is a material with a number of advantageous properties that strongly depend on its structure. In this study, bulk SiOC ceramics are prepared from polymer precursors with different side groups (Si–H, Si–CH<sub>3</sub>, Si–CH=CH<sub>2</sub>, and Si–C<sub>6</sub>H<sub>5</sub>) to understand the influence of the C content and network on the structures and properties of the resulting SiOC ceramics. The influence of the side groups on the thermophysical characteristics, phase evolution, oxidation resistance, and electrical conductivity of the SiOC materials is systematically studied. The SiOC samples show superior thermal stability in the air atmosphere up to 690–860 °C. The highest electrical conductivity is 705.3 S m<sup>-1</sup> at 403 °C, the highest to date for this family of materials and 3.5 times that of other reported studies. A new concept of free C connectivity is created to correlate with the electrical conductivity. This new conducting behavior with high thermal stability presents promising application potentials in high-temperature semi-conducting components.

## 1 Introduction

Polymeric precursors have been used to produce advanced ceramics at significantly lower temperatures than conventional powder processing. These precursors are polymers with a Si- and O-containing backbone, and can yield so-called polymer-derived ceramics (PDCs) via elimination of organic moieties. PDCs often contain amorphous phases (e.g., SiOC), in which nanocrystallites (such as SiC) and free C co-exist and the structure evolves with pyrolysis temperature [1]. Because of the formation of a homogeneous amorphous plus nanocrystalline mixed structure starting from polymer precursors containing Si–H, Si–CH<sub>3</sub>, Si–CH<sub>2</sub>CH<sub>3</sub>, Si–CH=CH<sub>2</sub>, and/or Si–C<sub>6</sub>H<sub>5</sub> bonds, SiOC is an exciting high-temperature material system that can produce a huge variety of compositions and

microstructures, depending on polymer precursors as well as crosslinking and pyrolysis conditions. It has received much attention in recent years because of the tailorable chemical and physical properties that can be achieved by varying starting polymer compositions and synthesis conditions, and has been studied as electrodes [2, 3], porous ceramics [4, 5], chemical reactors [6], fibers [7], lightweight structural materials [8], and gas storage media [1, 9].

SiOC ceramics can be expressed as SiO<sub>2(1-x)}</sub>C<sub>x</sub> + yC<sub>free</sub>, where x + y is the molar ratio of the C content relative to the Si content [10]. The compositions and structural characteristics of these materials change continuously with the precursors, the conditions used to process the precursors, and any fillers that might be employed [11]. The chemical compositions can be controlled by varying the molecular architecture of the organosiloxane precursors as well as the temperature and atmosphere of pyrolysis [12, 13]. Different C content influences the compositions, structural characteristics, phase changes, and subsequently performance of SiOCs. The free C, recognized for its turbostratic and/or graphitic nature, can be either advantageous or detrimental, depending on the specific application [14]. In inert atmospheres, the free C can be advantageous for the formation of SiC and other metal carbide phases via carbothermal reduction [10]. It can also improve thermal stability by inhibiting or retarding transitions from metastable states (oxycarbide phase) to more stable phases (SiC and SiO<sub>2</sub>) [11]. There is a growing

✉ Kathy Lu  
klu@vt.edu

<sup>1</sup> Key Laboratory of Applied Chemistry, College of Chemistry and Chemical Engineering, Bohai University, Jinzhou 121013, China

<sup>2</sup> Department of Materials Science and Engineering, Virginia Polytechnic Institute and State University, 117 Surge Building, Virginia Tech, Blacksburg, VA 24061, USA

<sup>3</sup> Department of Environmental Engineering, North China Institute of Science and Technology, Beijing 101601, China

interest in SiOC systems of high C content because of their high electrical conductivity and high permittivity as anode materials for lithium-ion batteries [15, 16], temperature sensors, MEMS devices, and conductive coatings [8]. Various C-rich SiOC ceramics have been reported to exhibit good electrochemical performance in terms of lithium insertion/extraction [17–19]. However, when the free C amount is excessive, thermal oxidation in oxidative atmospheres can quickly degrade the SiOCs.

Various methods were reported for tailoring the chemical compositions of SiOCs with a high C content. For example, Hourlier et al. [14] used aromatic crosslinker divinylbenzene (DVB) and introduced a significantly higher C content compared to tetramethyl-tetravinyl cyclotetrasiloxane (TMTVS). Crosslinking agents containing Si–CH=CH<sub>2</sub> were also used to initiate hydrosilylation reaction [20] and increase the C content even though to a lesser extent. However, the effects of side groups of polymer precursors in the preparation and properties of SiOC bulk ceramics have not yet been systematically studied.

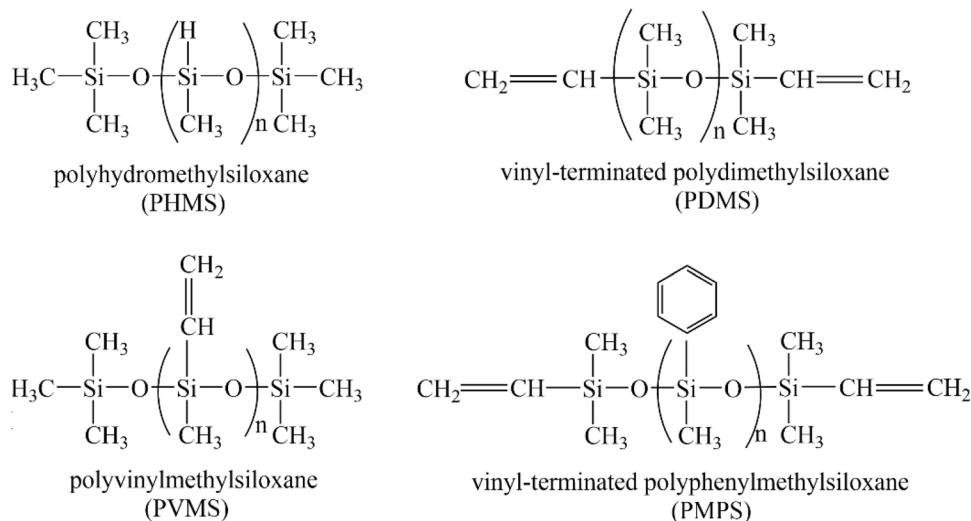
In this work, dense SiOC ceramics of varying C content were prepared using commercially available polysiloxanes. The ceramization, phase evolution, thermal stability, and electrical conductivity of different C-containing SiOC ceramics were studied. The influence of side groups (Si–H, Si–CH<sub>3</sub>, Si–CH=CH<sub>2</sub>, or Si–C<sub>6</sub>H<sub>5</sub>), pyrolysis temperature, and C content on the thermophysical properties, phase evolution, oxidation resistance, and electrical conductivity of the SiOC ceramics was systematically studied. The SiOC ceramics have been characterized using X-ray diffraction (XRD), Fourier transform infrared spectroscopy (FT-IR), thermogravimetric analysis (TGA), and Raman spectroscopy.

## 2 Experimental procedures

All the chemicals were obtained from Gelest Inc., Morrisville, PA, USA. They were all of analytical grade and were used without further purification. To investigate the effects of different C-containing side groups from precursors, polyhydromethylsiloxane (PHMS,  $M_w = 1400\text{--}1800$  g/mol, 20.00 wt% C in the monomer), vinyl-terminated polydimethylsiloxane (PDMS,  $M_w = 5000\text{--}7000$  g/mol, 32.43 wt% in the monomer), polyvinylmethylsiloxane (PVMS,  $M_w = 1000\text{--}1500$  g/mol, 41.86 wt% in the monomer), and vinyl-terminated polyphenylmethylsiloxane (PMPS,  $M_w = 2000\text{--}3000$  g/mol, 61.76 wt% in the monomer) were used as starting materials. These precursors contain different amounts of C due to the Si–H, Si–CH<sub>3</sub>, Si–CH=CH<sub>2</sub>, and Si–C<sub>6</sub>H<sub>5</sub> side groups involved (Fig. 1). 2.1–2.4 wt% platinum–divinyltetramethyldisiloxane complex in xylene was used as a catalyst.

PDMS–15 PHMS, PVMS–15 PHMS, and PMPS–15 PHMS samples were obtained by catalytic crosslinking of PDMS (or PVMS, or PMPS) and PHMS without using any solvent. The PDMS (PVMS or PMPS) to PHMS weight ratio was 85/15. First, solutions with the polymer precursor (PDMS or PVMS or PMPS) and PHMS were sonicated for 10 min and then mixed in a high-energy mill (SPEX 8000 M Mixer/Mill, SPEX Sample Prep, Metuchen, NJ, USA) for 10 min to form a homogeneous mixture. Next, the Pt catalyst (5 ppm relative to PHMS) was added, the mixtures were mixed again in the high-energy ball mill for 5 min, and then poured into aluminum foil molds. The mixtures were placed in a vacuum chamber and vacuumed for 10 min at 1500 mTorr to remove any bubbles in the solutions. The filled molds were then placed in an oven to crosslink at 50 °C for 12 h

**Fig. 1** Molecular structures of the polysiloxanes used in the study



and then at 120 °C for 6 h. When crosslinking PHMS, only 2.5 ppm of the above Pt catalyst solution was added to slow down the crosslinking and avoid defect formation; other steps were the same. The crosslinking for the PHMS samples was realized through the hydrolysis of the Si–H bonds and then H<sub>2</sub>O condensation (see Fig. 4).

To prepare the samples for pyrolysis, the cured materials were first cut and polished to roughly 13 mm × 13 mm × 3 mm size. Next, the samples were placed in a zirconia crucible between two graphite melts to reduce frictional forces due to the shrinkage of the green bodies during pyrolysis and allow for uniform outgassing of volatiles during ceramization. They were then put into a tube furnace (1730-20 Horizontal Tube Furnace, CM Furnaces Inc., Bloomfield, NJ). The samples were pyrolyzed in an Ar atmosphere with a flow rate of about 900 std cm<sup>3</sup>/min at 1000 °C, 1200 °C, 1300 °C, and 1400 °C, respectively, with a heating rate of 1 °C/min for 2 h, then cooled to 400 °C with a rate of 1 °C/min, and finally cooled to 50 °C with a rate of 2 °C/min. The pyrolyzed SiOC ceramic samples were named PHMS, PDMS–15PHMS, PVMS–15PHMS, and PMPS–15PHMS, respectively. Thus, four SiOC ceramics with different amounts of C were synthesized.

The bulk densities of the SiOCs were measured using the Archimedes method with water as the saturating and submersion medium. The phases were identified by XRD using an X'Pert PRO diffractometer (PANalytical B.V., EA Almelo, The Netherlands) with Cu K<sub>α</sub> radiation ( $\lambda$ ) 1.5406 (Å) at a scan rate of 0.03°/s. The chemical bonds were evaluated using FT-IR (Nicolet 8700 with Pike GladiATR attachment, ThermoScientific, Waltham, MA, USA), recorded between 400 and 4000 cm<sup>-1</sup> wavenumber with a resolution of 4 cm<sup>-1</sup>, and averaged between 64 scans. The thermal stability of the SiOC samples after pyrolysis was investigated using a STA 449C Jupiter<sup>®</sup> analyzer (Netzsch-Gerätebau GmbH, Selb, Germany) from room temperature to 980 °C at a heating rate of 5 °C min<sup>-1</sup> and an air flow of 40 ml·min<sup>-1</sup>. The electrical conductivity of the samples was measured by a four-point probe configuration using a potentiostat (VersaSTAT 3, Princeton Applied Research, Oak Ridge, TN, USA) in an Ar environment from room temperature up to 700 °C. The measurement voltage and current were automatically adjusted during the measurements. Raman spectra were recorded on a Horiba spectrometer (JY Horiba HR 800) with an excitation wavelength of 514 nm produced by an Ar laser. The 900–3500 cm<sup>-1</sup> spectral range was evaluated using ten scans for each measurement. To determine the peak positions and the integral intensities of different bands, spectral deconvolution was performed.

## 3 Results and discussion

### 3.1 Thermophysical properties

Photographs of the green samples after crosslinking are shown in Fig. 2a. After reacting for 6 h at 120 °C, the PHMS, PDMS–15PHMS, and PVMS–15PHMS mixtures transformed from viscous, transparent liquids into hard and transparent solid samples, while the PMPS–15PHMS formed a gel with a sticky, milky appearance. This difference after crosslinking is due to the highly disordered structure of the PMPS with the presence of the phenyl group, which serves as a barrier for polymer chain alignment. The milky appearance is due to the corresponding light scattering effect.

The SiOC ceramics after pyrolysis at different temperatures are black and defect free (free of cracks, voids, etc.) (as shown in Fig. 2b). The unpolished surfaces are smooth and light reflecting, and the polished surface is totally black. Table 1 shows the volume shrinkage, ceramic yield, and bulk density values for the four samples after pyrolysis. The volume shrinkage for all the samples is in the range of 42.7–59.4%. For the same sample, there is no significant shrinkage difference with the pyrolysis temperature. At the same pyrolysis temperature, the volume shrinkage increases when the C content in the precursor increases. The ceramic yield values for all the samples range from 74.5 to 84.5%. At the same pyrolysis temperature, an increase in the precursor C content results in a decrease in the ceramic yield. For the same C content, the ceramic yield has no obvious change with the pyrolysis temperature increase.

The changes of the ceramic yield and volume shrinkage are related to the pyrolysis process. At low pyrolysis temperatures (800–1100 °C), the SiOC consists of a homogeneous network of mixed Si–O–C tetrahedra and free C species [12]. During the pyrolysis at 1100–1400 °C, main reactions take place as follows [21]:

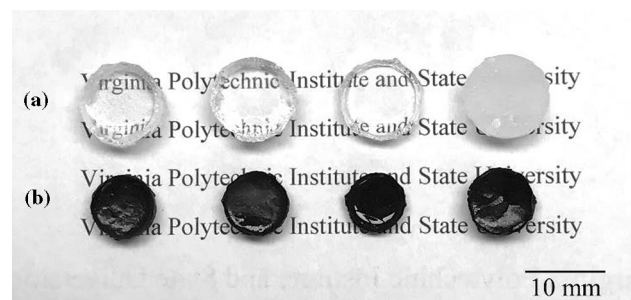
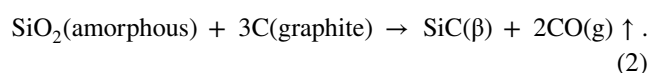
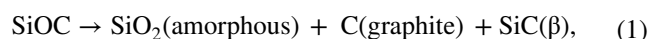


**Fig. 2** Photographs of as-crosslinked (a) and pyrolyzed (b) samples. From left to right: PHMS, PDMS–15PHMS, PVMS–15PHMS, and PMPS–15PHMS

**Table 1** Volume shrinkage, ceramic yield, and density of the SiOC samples after 1000–1400 °C pyrolysis

	PHMS (20.00 wt% C)	PDMS–15PHMS (30.57 wt% C)	PVMS–15PHMS (38.58 wt% C)	PMPS–15PHMS (55.50 wt% C)
Volume shrinkage (%)				
1000 °C	43.70 ± 2.35	50.23 ± 1.54	57.12 ± 1.01	59.40 ± 3.23
1200 °C	44.69 ± 1.20	52.31 ± 0.56	56.09 ± 0.23	56.32 ± 0.09
1300 °C	42.73 ± 2.15	51.24 ± 0.78	58.21 ± 1.30	58.56 ± 2.40
1400 °C	44.25 ± 0.39	51.23 ± 1.45	58.45 ± 0.47	59.11 ± 0.03
Ceramic yield (%)				
1000 °C	83.56 ± 1.74	79.12 ± 0.56	79.42 ± 0.65	78.96 ± 0.85
1200 °C	80.29 ± 2.10	79.26 ± 0.78	77.41 ± 0.87	79.05 ± 1.20
1300 °C	84.56 ± 0.29	75.03 ± 1.21	78.65 ± 0.45	78.64 ± 1.13
1400 °C	83.43 ± 0.65	74.59 ± 2.43	78.42 ± 2.10	74.50 ± 1.65
Density <sup>a</sup> (g·cm <sup>-3</sup> )				
1000 °C	1.86 ± 0.02	1.75 ± 0.02	1.82 ± 0.02	1.80 ± 0.02
1200 °C	1.85 ± 0.02	1.78 ± 0.02	1.56 ± 0.02	1.58 ± 0.02
1300 °C	1.88 ± 0.02	1.85 ± 0.02	1.68 ± 0.02	1.59 ± 0.02
1400 °C	1.94 ± 0.02	1.83 ± 0.02	1.60 ± 0.02	1.64 ± 0.02

<sup>a</sup>Estimated error using the Archimedes method

Equation (1) represents the SiOC phase separation into amorphous SiO<sub>2</sub>, SiC(β), and graphite (~1300 °C). Equation (2) indicates that at  $T > 1300$  °C, a carbothermal reaction occurs between SiO<sub>2</sub> and graphite, producing SiC(β) and CO gas. When introducing more C into the sample (PVMS or PMPS), the vinyl or phenyl groups lead to more volatile species and pyrolyze into more free C at high temperatures. Higher C formation in general leads to lower ceramic yield and higher volume shrinkage. Therefore, for the same composition, increasing pyrolysis temperature leads to more SiC formation and CO release, thus the ceramic yield decreases and the volume shrinkage increases. Due to the simultaneous phase evolution and evaporative species loss, the volume shrinkage and ceramic yield show large variations.

The densities for all the SiOC samples are in the range of 1.56–1.94 g cm<sup>-3</sup>. At the same pyrolysis temperature, higher C content generally leads to lower bulk density (except for 1000 °C, at which the reactions according to Eqs. (1) and (2) are not extensive yet). This indicates that there is indeed more weight loss for higher C content samples, the impact is significant enough to affect the resulting densities at 1200–1400 °C. In general, with an increase in the C content, the volume shrinkage increases, the ceramic yield decreases, and the bulk density decreases in the wide temperature range of 1200–1400 °C, even though measurement errors in sample dimensions introduce some inconsistency to this trend. This means that the increased C content in the precursors leads to more mass loss but higher free C content in the SiOC ceramics. Again, the simultaneous mass loss and phase evolution mean that the density change is not strictly linear.

### 3.2 Structural evolution

The FT-IR results of the crosslinked materials are shown in Fig. 3. All the samples show sharp peaks at approximately 750–865, 1256, and 2965 cm<sup>-1</sup>, characteristic of the Si–CH<sub>3</sub> group, and a broad peak in the 1000–1100 cm<sup>-1</sup> range which can be assigned to Si–O–Si [22]. For the PHMS sample, the main absorption bands are associated with the Si–H bond (2160 cm<sup>-1</sup>), in addition to the Si–CH<sub>3</sub> and Si–O–Si groups [2]. Compared to the other samples, the PHMS sample has

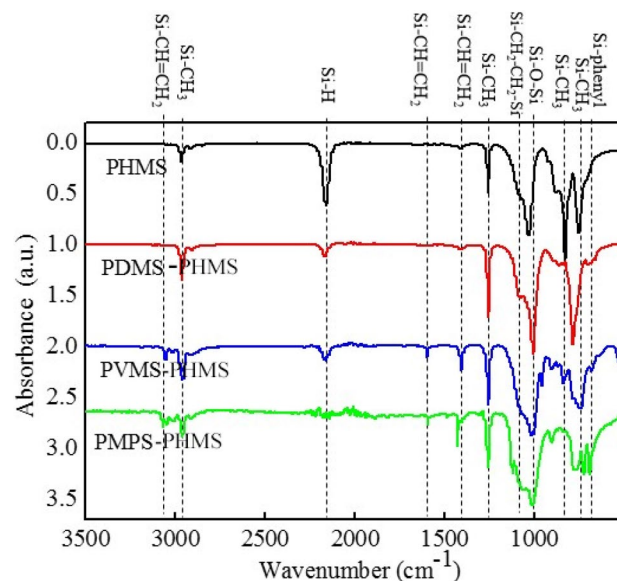


**Fig. 3** FT-IR spectra of the PHMS, PDMS–15PHMS, PVMS–15PHMS, and PMPS–15PHMS after crosslinking

the highest intensity of the Si–H group. The crosslinking process for the PHMS sample is shown in Fig. 4a. We believe that with the presence of moisture ( $\text{H}_2\text{O}$  species) in air, PHMS undergoes partial hydrolysis to produce PHMS–OH [23]. Poly-condensation crosslinking occurs between the PHMS and OH species and produces crosslinked PHMS,  $\text{H}_2\text{O}$ , and  $\text{H}_2$  gas. The  $\text{H}_2$  and  $\text{H}_2\text{O}$  evolution at this stage is associated with dehydrocoupling reactions between two

Si–OH groups, and between Si–H and Si–OH, according to Eqs. (3) and (4) [14]:

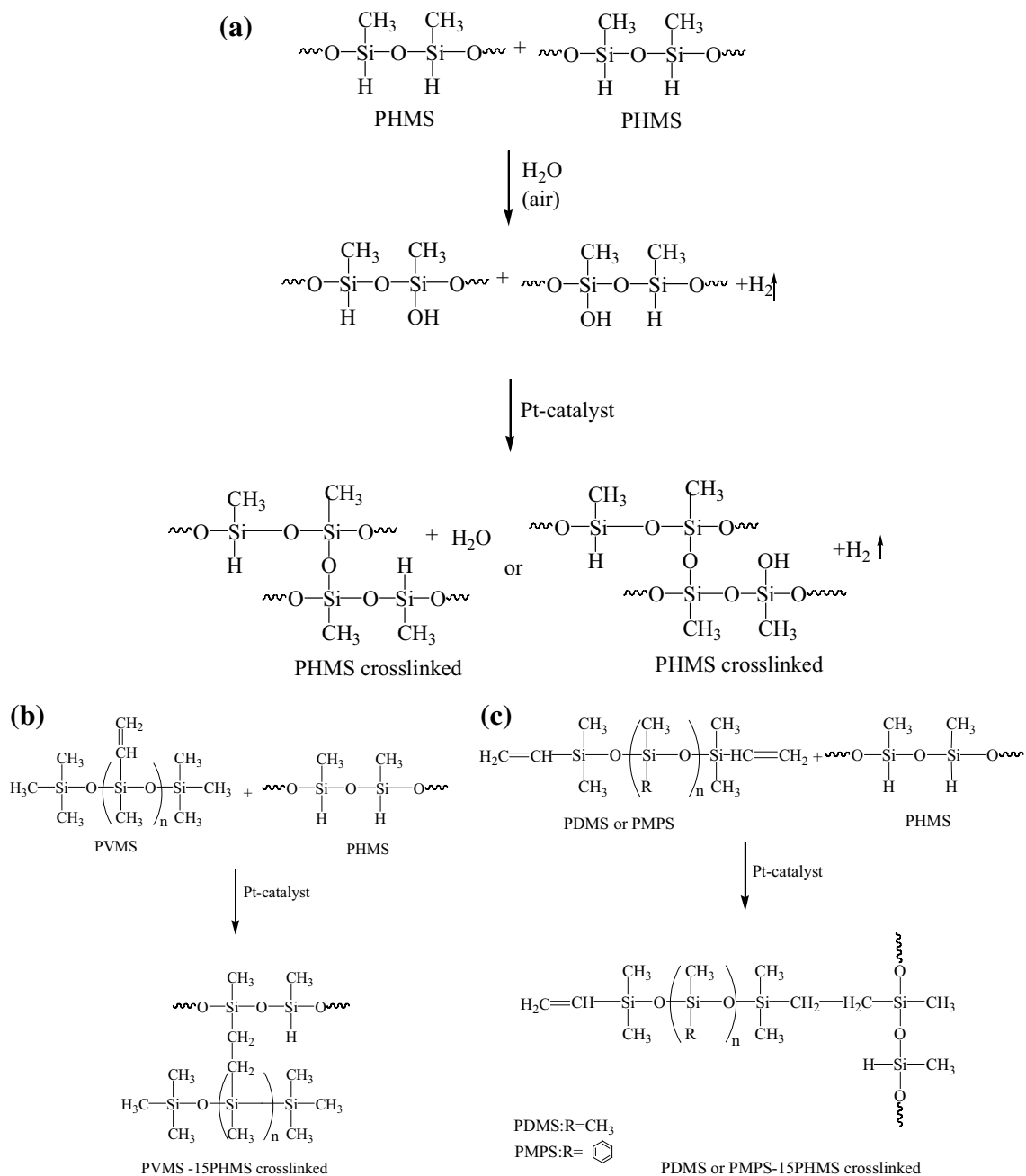
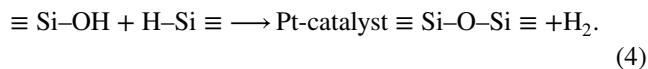
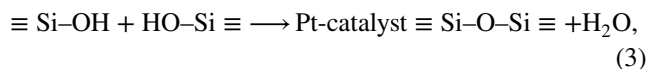
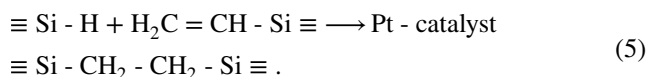


**Fig. 4** Schematic representation of **a** PHMS crosslinking, **b** PVMS–15PHMS crosslinking, and **c** PDMS–15PHMS or PMPS–15PHMS crosslinking

The band at  $2160\text{ cm}^{-1}$  is typical of  $\nu(\text{Si-H})$  absorption, suggesting that part of PHMS still remains in the crosslinked network, due to incomplete hydrolysis. For the PVMS, PDMS, and PMPS samples, the main absorption bands are associated with  $\text{Si-CH=CH}_2$  ( $1400$ ,  $1600$ , and  $3060\text{ cm}^{-1}$ ), and the shoulder peak is assigned to  $\text{Si-CH}_2\text{-CH}_2\text{-Si}$  ( $1120\text{--}1180\text{ cm}^{-1}$ ) [24]. In addition, only the PMPS sample demonstrates extensive Si-phenyl bonding at  $694$  and  $730\text{ cm}^{-1}$  [22]. Compared to the intensity of the  $\text{Si-CH=CH}_2$  peak in Fig. 3, the  $\text{Si-CH=CH}_2$  peak of the PDMS sample is very weak. We believe this is because the molecular weight of the PDMS is relatively large and only a small amount of terminated vinyl groups exists. During the crosslinking process, most of the vinyl groups in PDMS are involved in the reaction, thus the remaining unreacted vinyl groups are negligible. The main chemical bonds found in the FT-IR spectra of the crosslinked polymers are summarized in Table 2.

Hydrosilylation reaction is often used for modifying silicon-based polymers. Si-H groups within the polymer backbone can easily react with vinyl groups of the precursors, as represented below [25]:



Due to the large number of available building blocks, including monomers, oligomers, and polymers, a wide variety of precursors can be employed in this strategy [25]. Hydrosilylation reaction is a versatile reaction that provides many benefits in relation to other crosslinking mechanisms. It can occur at room temperature in the presence of a catalyst. In this work, the  $\text{Si-CH=CH}_2$  of PDMS (or PVMS, PMPS) reacts with the Si-H bond in PHMS to produce a three-dimensional network structure and thus a higher ceramic yield. The ceramic yield values ( $74.5\text{--}78.4\%$ ) for the PDMS-15PHMS, PVMS-15PHMS, and PMPS-15PHMS

are higher than those reported in the literature ( $66.5\text{--}71.9\%$ ) under the same conditions [13]. Figure 4b, c shows the reactions between PDMS (PVMS, PMPS) and PHMS, giving rise to hydrosilylation of the vinyl functional group with the Si-H-containing compounds.

Figure 5 shows the XRD patterns of different SiOC ceramics pyrolyzed at different temperatures. At a lower temperature of  $1000\text{ }^\circ\text{C}$ , small peaks centered at  $26.2^\circ$  and  $44.4^\circ$  are indexed to be graphite (JCPDS Card no. 00-075-1621) in Fig. 5a [26]. The XRD patterns of all the samples (PHMS, PDMS-15PHMS, PVMS-15PHMS, and PMPS-15PHMS) pyrolyzed at  $1000\text{ }^\circ\text{C}$  show an amorphous structure with only the presence of the  $\text{SiO}_2$  halo centered at  $\sim 22^\circ$  and the SiC peak at  $35.7^\circ$  [27], which means that the phase separation is about to happen. However, the tiny XRD peaks cannot indicate phase separation difference among the samples.

Figure 5b shows the XRD patterns of the SiOC samples pyrolyzed at  $1200\text{ }^\circ\text{C}$ . All the samples exhibit a very broad peak at  $\sim 22^\circ$ , which is attributed to the presence of amorphous  $\text{SiO}_2$ . The peaks centering at  $35.7^\circ$ ,  $41.5^\circ$ ,  $60.1^\circ$ , and  $71.9^\circ$  are indexed to be  $\beta\text{-SiC}$  (JCPDS Card no. 01-073-1665) in the PMPS-15PHMS sample, indicating that the crystallization of  $\beta\text{-SiC}$  is promoted with an increasing C content. The small peaks centering at  $26.2^\circ$  and  $44.4^\circ$  are indexed to be graphite. For the other three samples (low C content), the phase separation is less obvious, especially for the PHMS and PDMS-15PHMS samples. This means that the phase separation takes place at  $1000\text{--}1200\text{ }^\circ\text{C}$  in the high-C content samples, earlier than the low-C content samples. Excessive C accelerates the formation of graphitic carbon and the onset of SiC crystallization [24].

Figure 5c shows the XRD patterns of the SiOC samples pyrolyzed at  $1300\text{ }^\circ\text{C}$ . All the samples exhibit a very broad peak at  $\sim 22^\circ$ , which again is attributed to amorphous  $\text{SiO}_2$ , and the shoulder peaks centering at  $26.2^\circ$  and  $44.4^\circ$  are indexed to be graphite. The diffraction peaks at  $35.7^\circ$ ,  $41.5^\circ$ ,  $60.1^\circ$ , and  $71.9^\circ$  correspond to the (111), (200), (220), and (311) crystalline planes of the  $\beta\text{-SiC}$  phase. The  $\text{SiO}_2$ , SiC, and graphite diffraction peaks appear due to the phase separation of SiOC, as well as the carbothermal reduction of  $\text{SiO}_2$  into SiC by Eqs. (1) and (2). With further pyrolysis temperature increase, the  $\beta\text{-SiC}$  peaks become more intense, indicating an enhancement of  $\beta\text{-SiC}$  crystallization. This is because the temperature increase, another important parameter influencing SiC crystallization, promotes the carbothermal reaction and generates more SiC( $\beta$ ) [28–30].

With the pyrolysis temperature increase from  $1300$  to  $1400\text{ }^\circ\text{C}$ , the  $\text{SiO}_2$  peak remains broad in all the samples (Fig. 5c, d), indicating that the domain structure is still highly disordered up to  $1400\text{ }^\circ\text{C}$ . The formation of

**Table 2** Major FT-IR peaks identified in the crosslinked polymers

Wavenumber ( $\text{cm}^{-1}$ )	Functional group	References
694	Si-phenyl	[22]
730	Si-phenyl	[22]
750–865	Si- $\text{CH}_3$	[22]
1000–1100	Si-O-Si	[22]
1120–1180	Si- $\text{CH}_2\text{-CH}_2\text{-Si}$	[24]
1256	Si- $\text{CH}_3$	[22]
1400	Si- $\text{CH=CH}_2$	[24]
1600	Si- $\text{CH=CH}_2$	[24]
2160	Si-H	[2]
2965	Si- $\text{CH}_3$	[22]
3060	Si- $\text{CH=CH}_2$	[24]

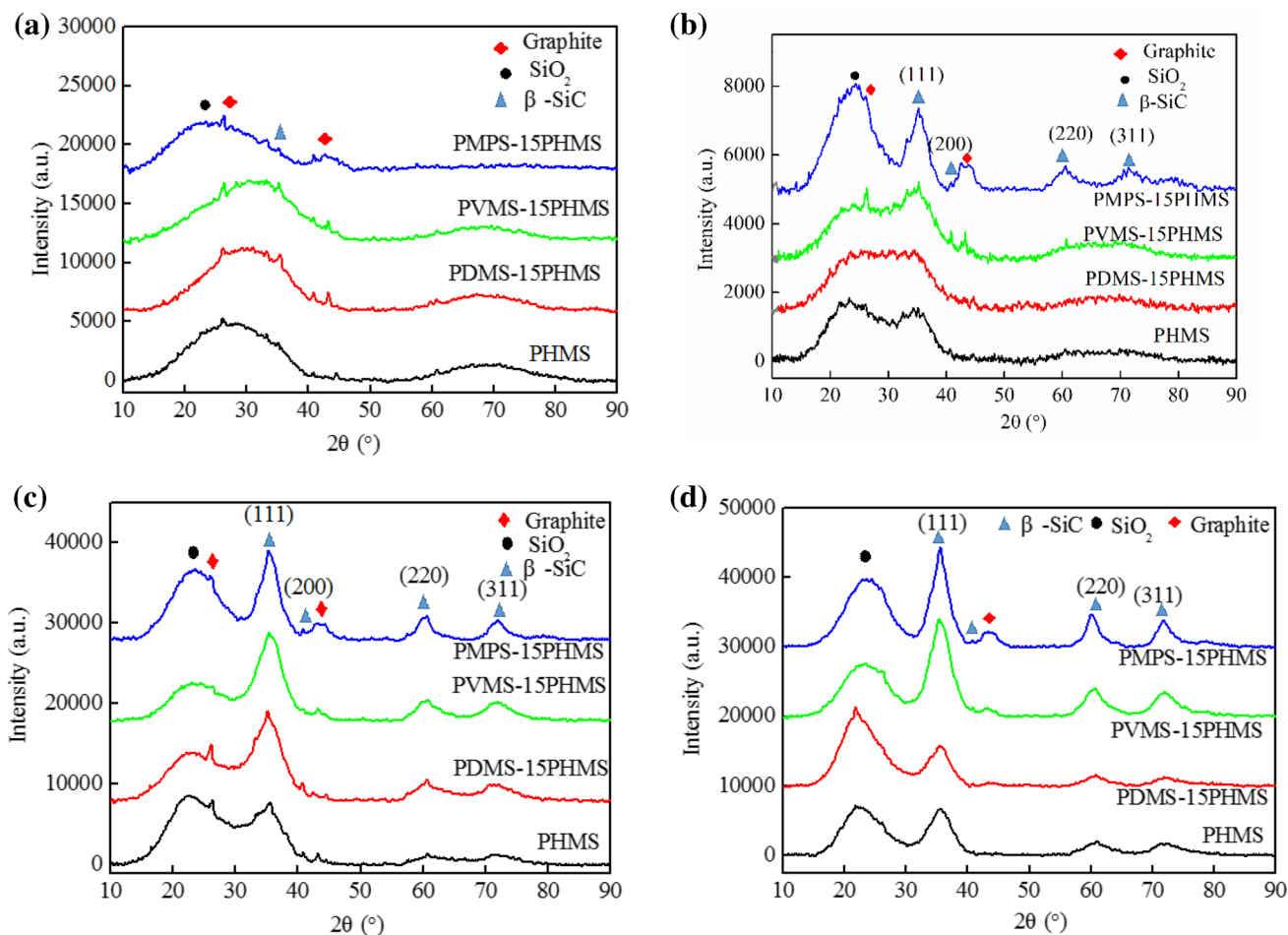
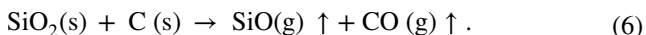
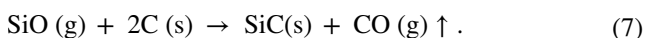


Fig. 5 XRD patterns at different pyrolysis temperatures: a 1000 °C, b 1200 °C, c 1300 °C, and d 1400 °C

crystalline SiO<sub>2</sub> is believed to be hindered by turbostratic C layers [26]. This is because at higher temperatures ( $T > 1300\text{ °C}$ ), the carbothermal reduction of SiO<sub>2</sub> can take place at a low content of free C, by consuming the C phase [25]:



This reaction results in the evaporation of CO and SiO gaseous species. At  $T > 1300\text{ °C}$  with high C contents, SiC(s) and CO(g) are the major decomposition products according to



Equations (6) and (7) show that the C contents play an important role in the reduction of SiO<sub>2</sub>. With a higher C content, the carbothermal reduction of SiO<sub>2</sub> produces more SiC, as observed for the PMPS-15PHMS and PVMS-15PHMS samples.

### 3.3 Thermal stability

SiOC is known for its thermal stability in inert atmospheres up to 1300 °C [8]. In this study, the major focus on the thermal stability is for air atmosphere, which is oxidative. The obtained TGA curves are presented in Fig. 6, which shows the mass change as a function of testing temperature. At 1400 °C pyrolysis temperature, the PHMS, PDMS-15PHMS, and PVMS-15PHMS samples are stable up to 864 °C (taking 2 wt% change as the cutting point) before a gradual weight gain up to 6.2, 3.5, and 4.7 wt%, respectively, at 1000 °C. The main weight gain occurs above 800 °C. For the PMPS-15PHMS sample, however, the sample is stable up to 691 °C before a drastic weight loss for the 1400 °C pyrolysis condition, ~20 wt% at 980 °C. This means that with the high C content in this system, the thermal stability decreases significantly.

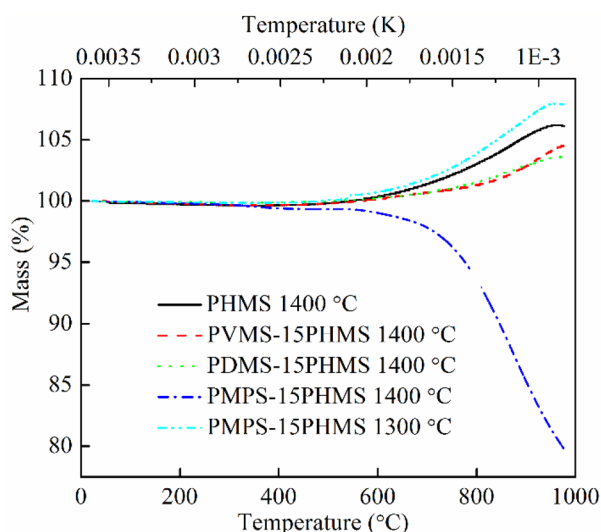
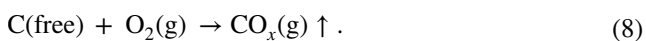


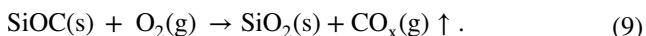
**Fig. 6** TGA curves for the SiOCs of different precursor compositions and pyrolysis temperatures

At 1300 °C pyrolysis temperature, the PMPS–15PHMS sample is stable up to 708 °C before a weight gain of ~8.0 wt%, with the same trend as for the PHMS, PDMS–15PHMS, and PVMS–15PHMS samples after 1400 °C pyrolysis. This is because the oxidative thermal degradation of the studied SiOC materials is related to phase separation, which is directly related to the pyrolysis temperature [31]. For the PMPS–15PHMS sample, lower pyrolysis temperatures (e.g., 1300 °C) lead to less phase separation, and higher pyrolysis temperatures (e.g., 1400 °C) lead to more extensive separation and thus less stable SiOC microstructures [8].

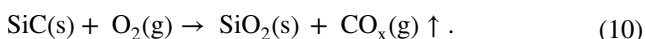
Based on the SiOC compositions, there are three unstable sources—free C, SiOC clusters, and SiC. For the free C, tiny graphene layers with edge C atoms can be oxidized; the radical species on the surface of free C can also be easily oxidized [32]. In the 400–800 °C range, the specific oxidation mechanism is the combustion of the free C phase [33]:



At 800–1000 °C, it can be represented as



At temperatures > 1000 °C, SiC can be oxidized according to [31]



Equation (8) leads to weight loss. Equation (9) causes the SiOC units to become more vulnerable to oxidation although it could lead to weight gain. Similarly, SiC oxidation could lead to weight gain. The low-C content

samples (PHMS, PDMS–15PHMS, and PVMS–15PHMS) show lower overall weight gain and indicate that SiOC or SiC oxidation is more dominant according to Eqs. (9) and (10). The high-C content sample (PMPS–15PHMS) shows higher weight loss at 1400 °C, meaning a higher amount of free C can be easily oxidized according to Eq. (8). As one of these phases (e.g., C) becomes unstable, it creates a more vulnerable system for thermal degradation due to the simultaneous oxidation of the free C and SiOC [8]. The low SiOC content is not effective for the formation of a protective SiO<sub>2</sub> layer [34].

Based on the thermal stability results in Fig. 6, the SiOC materials are relatively stable up to 800 °C in air atmosphere. The mixed bond structure of the SiOC and the free C network play a key role in the thermal stability of these ceramics [35].

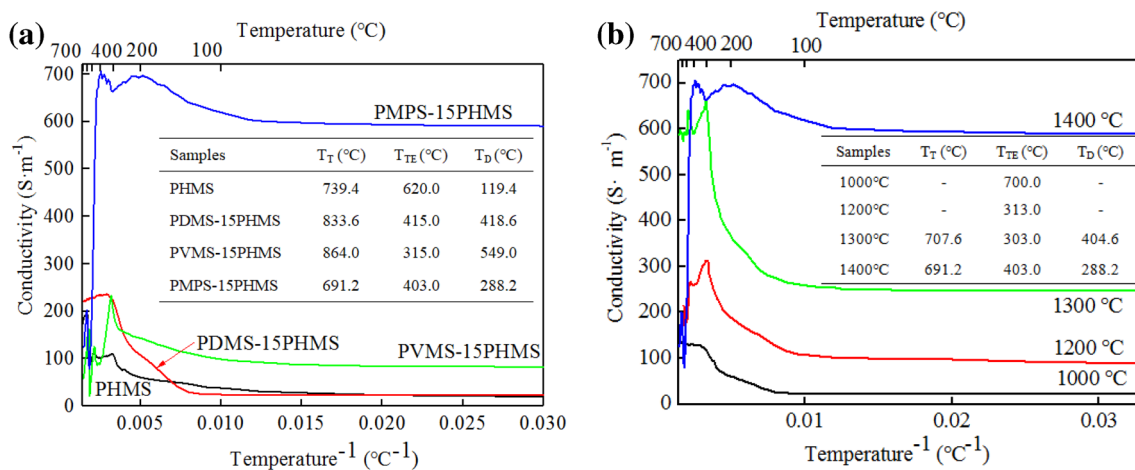
### 3.4 Electrical conductivity

Figure 7 presents the electrical conductivity results for the different samples pyrolyzed at 1400 °C and for the PMPS samples pyrolyzed at different temperatures. Both the inverse of the temperature in °C<sup>-1</sup> and the temperature in °C are provided as the x-axis for viewing convenience. Figure 7a shows the electrical conductivity change with the measurement temperature for the 1400 °C pyrolyzed samples. The PHMS, PDMS–15PHMS, and PVMS–15PHMS samples have much lower electrical conductivity compared to the PMPS–15PHMS sample. The conductivity increases from 18.7 S·m<sup>-1</sup> at room temperature to 198.2 S·m<sup>-1</sup> at 620 °C for the PHMS. For the PDMS–15PHMS sample, the conductivity increases from 23.3 S·m<sup>-1</sup> at room temperature to 234.6 S·m<sup>-1</sup> at 415 °C. For the PVMS–15PHMS sample, the conductivity increases from 81.4 S·m<sup>-1</sup> at room temperature to 232.8 S·m<sup>-1</sup> at 315 °C. For the PMPS–15PHMS sample, the conductivity increases from 590.2 S·m<sup>-1</sup> at room temperature to 705.3 S·m<sup>-1</sup> at 403 °C before dropping significantly.

Figure 7b shows the electrical conductivity change with the pyrolysis temperature for the PMPS–15PHMS sample. Higher pyrolysis temperatures lead to higher electrical conductivity. At 1000 °C pyrolysis temperature, the conductivity increases from 22.5 S·m<sup>-1</sup> at room temperature to 140.4 S·m<sup>-1</sup> at 700 °C. At 1200 °C pyrolysis temperature, it increases from 89.1 S·m<sup>-1</sup> at room temperature to 313.6 S·m<sup>-1</sup> at 313 °C. At 1300 °C pyrolysis temperature, the increase is from 246.7 S·m<sup>-1</sup> at room temperature to 664.2 S·m<sup>-1</sup> at 303 °C. At 1400 °C, the conductivity increases from 590.2 S·m<sup>-1</sup> at room temperature to 705.3 S·m<sup>-1</sup> at 403 °C before dropping significantly.

Among all the samples studied, the highest electrical conductivity is 705.3 S·m<sup>-1</sup>. This is the highest value ever reported for this family of SiOC materials, 52% higher





**Fig. 7** **a** Electrical conductivity curves for the SiOCs pyrolyzed at 1400 °C with different C contents, and **b** electrical conductivity change with pyrolysis temperature for the PMPS-15PHMS sample. The inserts show the degradation temperatures under

different conditions ( $T_T$  thermal degradation temperature,  $T_{TE}$  thermal + electric degradation temperature,  $T_D$  degradation temperature decrease under the electrical field)

**Table 3** Comparison of the electrical conductivity of several SiOC ceramics

Type of SiOC ceramics	Conductivity ( $S\ m^{-1}$ )	References
PMPS-15PHMS (1400 °C pyrolysis)	705.3 (403 °C)	Present study
PMPS-15PHMS (1300 °C pyrolysis)	664.2 (303 °C)	Present study
PVMS-15PHMS (1400 °C pyrolysis)	232.8 (315 °C)	Present study
PDMS-15PHMS (1400 °C pyrolysis)	234.6 (415 °C)	Present study
PHMS (1400 °C pyrolysis)	198.2 (620 °C)	Present study
SiOC (80 wt% DVB)	464.0 (350 °C)	[8]
SiOC-TiC <sub>x</sub> O <sub>y</sub> (30 wt% TiO <sub>2</sub> )	503.0 (400 °C)	[32]
SiC (at 1400 °C pyrolysis temperature)	0.31 (R.T.)	[39]
SiOC (1400 °C pyrolysis)	7.1 (R.T.)	[38]
SiOC (sintered at 1550 °C)	200.0 (300 K)	[36]
PMS (at 1400 °C pyrolysis temperature)	1.0 (1500 °C)	[37]
PPS (at 1400 °C pyrolysis temperature)	100.0 (1500 °C)	[37]
Turbostratic C and graphite	1-10 <sup>5</sup> (R.T.)	[40]
Polyorganosiloxane-divinylbenzene (50 wt%) (1100 °C pyrolysis)	2.3 (R.T.)	[41]

than what was reported in our earlier work [8] and at least 3.5 times of other reported values [36, 37]. The electrical conductivities of several SiOC ceramics are listed in Table 3, including the promising ones in this study. All the other reported results are considerably lower than that of the PMPS-15PHMS at  $\geq 1300$  °C pyrolysis condition. For the same pyrolysis temperature of 1400 °C, the conductivity of our samples is at least two orders of magnitude higher than the reported values [38].

Figure 7a, b also shows that for all the samples, the electrical conductivity increases up to a peak temperature before decreasing drastically. At the beginning of the measurement, as the temperature increases, the conductivity increases. This is believed to result from the electric

field-assisted ordering of the C phase [42, 43]. The sudden increase followed by the sharp drop in electrical conductivity is related to the further phase separation of SiOC into free C and SiC crystallites [8, 32]. Since the electrical conductivity has been conducted in Ar, the oxidation based on Eqs. (8) and (9) can be eliminated. With the simultaneous presence of high temperature and electrical field, the SiOC structure is destabilized. With the significant reorganization of the microstructure and species, the electrical conducting path is destroyed.

Assuming that the peak electrical conductivity temperature can be used as an indicator of the SiOC stability under an electric field at elevated temperatures, the impact of the electric field on the degradation acceleration can be shown

as listed in Fig. 7. Since the measurement was carried out in an Ar atmosphere, SiOC oxidation degradation effect can be ignored. As it shows, the electric field accelerates the SiOC degradation (through accelerated phase separation) by 119–549 °C. Compared to our earlier electrical conductivity measurement in air at elevated temperatures [8, 32], the electrical field has a dominant effect on the degradation of the SiOC thermal stability.

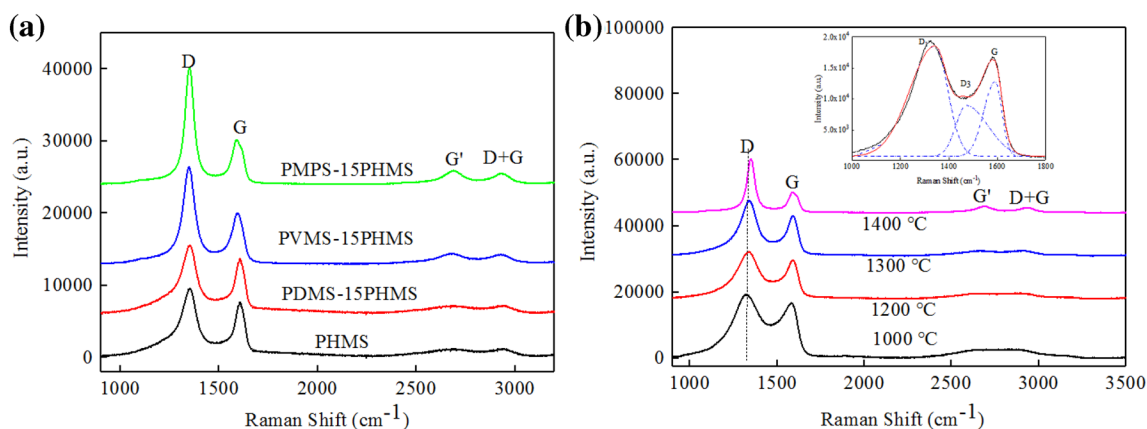
Among the phases present in the SiOC samples (C, SiO<sub>2</sub>, SiOC, and SiC), free C should be the conducting phase. However, free C can exist as amorphous C, turbostratic C, and graphitic C. To better understand the influence of the specific C species on the electrical conductivity, the change of the C contents in the SiOC materials has been evaluated using Raman spectroscopy and presented in Fig. 8.

Figure 8a shows the Raman spectra of the SiOC samples at 1400 °C pyrolysis temperature. The D band locating at ~1350 cm<sup>-1</sup> is ascribed to the defects and disordering in the free C, whereas the G band (in-plane vibrational mode) at 1592–1606 cm<sup>-1</sup> is attributed to the ordered graphitic structure [44]. The broad G' band at 2682 cm<sup>-1</sup> and the weak band around 2934 cm<sup>-1</sup> can be assigned to a combination of the defect/disordering and graphitic mode (G+D), which are observed for the PVMS–15PHMS and PMPS–15PHMS samples. The D and G peaks shift to lower vibrational frequencies and there is a reduction in the full width at half maximum (FWHM) of the D band with an increasing C content. As a general rule, the more s-character in a hybridized orbital will lead to a stronger bond, shorter bond length, and higher wavenumber in the Raman spectrum. A sp<sup>2</sup>-hybridized orbital contains 33.33% s-character and a sp<sup>3</sup>-hybridized orbital contains 25% s-character. Thus, the G band (sp<sup>2</sup>) shows a higher wavenumber than the D bond. With an increasing carbon content in the SiOC system, a more disordered carbon structure will form, which is

consistent with the increasing intensity of the D bond. With less sp<sup>2</sup>-hybridized orbitals and the s-character, a weaker bond will form, which means that the longer bond length will cause the Raman peak to shift to a lower wavenumber.

Figure 8b shows the Raman spectra of the PMPS–15PHMS samples obtained at different pyrolysis temperatures. The free C phase of the SiOC samples displays the typical spectrum of highly disordered C with broad and strongly overlapped D and G bands. With the pyrolysis temperature increase, the free C phase undergoes reorganization to form more ordered C from 1000 to 1300 °C. To determine the peak positions and the integral intensities of different bands, Raman peak deconvolution has been performed. The fitted spectra (Fig. 8b insert, using the Gaussian function in the Raman spectroscopy software) illustrate three contributions centered at around 1345, 1500, and 1595 cm<sup>-1</sup>. The two intense, broad bands at 1345 and 1595 cm<sup>-1</sup> are related to the D<sub>1</sub> (turbostratic C) and G bands (ordered C) of polycrystalline graphite, whereas the D<sub>3</sub> band at 1500 cm<sup>-1</sup> indicates the presence of amorphous C in the samples [45–47]. When the pyrolysis temperature increases to 1400 °C, the broad G' band at 2682 cm<sup>-1</sup> and the weak band around 2934 cm<sup>-1</sup> can be assigned to a combination of the graphitic and disordered C (G+D). The D<sub>1</sub> and G peaks shift to higher vibrational frequencies and there is a reduction of the D and G band widths with increasing pyrolysis temperature. This is because with increasing pyrolysis temperature, an enhancement of turbostratic C crystallization occurs, which means the s-character will increase due to the more sp<sup>2</sup>-hybridized structure. The stronger bond (the higher energy of the sp<sup>2</sup> bonds) pushes the vibrational frequency of the bonds higher and hence the wavenumber of the bond in the Raman spectrum goes higher.

The structural evolution of the free C phase dispersed in the SiOC ceramics can be quantified based on the XRD



**Fig. 8** Raman spectra of **a** SiOCs at 1400 °C pyrolysis and **b** PMPS–15PHMS at different pyrolysis temperatures. The insert in **b** shows the deconvoluted spectra of the PMPS–15PHMS sample pyrolyzed

at 1000 °C (the deconvoluted spectra of the PMPS–15PHMS sample pyrolyzed at 1200 °C, 1300 °C, and 1400 °C are similar to what is shown in the insert)

and Raman spectroscopy results (Figs. 5, 8). The integrated area percent of the XRD patterns for free C (44.4°) and SiC (35.7°, 60.1°, 71.9°) of each sample pyrolyzed at different temperatures can be used for comparison purpose. At the pyrolysis temperature of 1400 °C, the PHMS and PDMS–15PHMS samples have much lower turbostratic and graphitic C compared to the PVMS–15PHMS and PMPS–15PHMS samples. The graphitic C is 1.87, 2.10, 7.95, and 11.37 wt% for the PHMS, PDMS–15PHMS, PVMS–15PHMS, and PMPS–15PHMS samples, respectively. The turbostratic C is 3.57, 4.74, 18.44, and 27.39 wt% for the PHMS, PDMS–15PHMS, PVMS–15PHMS, and PMPS–15PHMS samples, respectively. At the same time, the SiC content fluctuates. The free C phase embedded within the matrix increases the electrical conductivity compared to SiO<sub>2</sub> [48]. Previous structural studies have shown that besides bonding to silicon, the majority of the C species are bonded to other C atoms to form nanodomains of sp<sup>2</sup> free C, existing as turbostratic C or graphene-like sheets [49]. A well-dispersed free C phase is believed to be composed of turbostratic C and graphene-like C. Both C phases appear to be tightly bonded to the glassy matrix [44, 48]. The contents of the turbostratic and graphitic C and the interconnectivity of the C network are believed to exert a major influence on the electrical conductivity. High fractions of the turbostratic C (~27.39 wt%) and ordered C (~11.37 wt%) with sp<sup>2</sup> hybridization result in high conductivities for the pyrolyzed PMPS–15PHMS [40]. For the PHMS and PDMS–15PHMS, the lower conductivity is contributed to the lower free C content (5.44–26.39 wt%). However, SiC does not seem to have an impact on the electrical conductivity due to its discrete distribution in the SiOC matrix, resulting from the lower amount.

As expected, both turbostratic and graphitic C contents increase as the C content in the polymer precursors increases. However, the SiC content fluctuates with the polymer precursor change but with no direct correlation with either the free C or the polycrystalline C content (overlapping with each other due to the absence of the

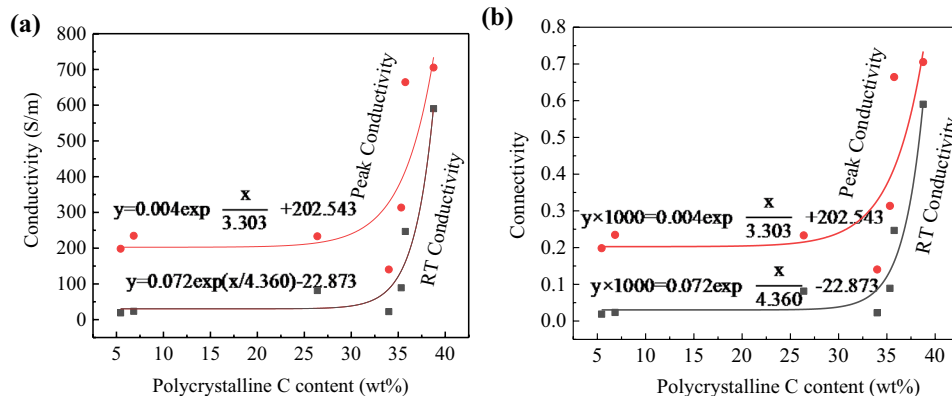
amorphous C). The specific SiC content is related to the intrinsic pyrolysis behavior of the polymer precursors. This means that the polycrystalline carbon is the deciding factor for the electrical conductivity. With the C content increase in the polymer precursor side group, the polycrystalline carbon content increases, which in turn leads to higher electrical conductivity for the pyrolyzed SiOC. Even with the pyrolysis temperature increase and continuous phase separation, the turbostratic C and graphitic C contents still increase. The only decrease is the amorphous C content, which also leads to free carbon content decrease. Thus, the total free carbon amount is not an effective gauge of the electrical conductivity. It also shows that the SiC formation is inversely proportional to the amorphous C content. The C species in SiC comes from the amorphous C. When the C species evolve into bonded C species (both turbostratic C and graphitic C), the tendency to bond with Si greatly diminishes and is unlikely to form SiC.

For the same sample, the amount of free C decreases with the pyrolysis temperature increase. Although the free C content decreases due to the sharp decrease caused by the amorphous C decrease, the turbostratic C and ordered C contents increase. From the Raman peak analysis, the increase in the electrical conductivity of the SiOC ceramics with increasing pyrolysis temperature is attributed to an increase in the sp<sup>2</sup> C bonds. A high fraction of C with sp<sup>2</sup> hybridization results in high conductivities of the pyrolyzed SiOC materials. Clearly, the total C content is not an effective parameter for the electrical conductivity prediction.

C nanofibers are composed of a mixture of defective C (corresponding to the turbostratic C in this study) and graphitic C. On average, the electrical conductivity is ~1000 S·m<sup>-1</sup> [50–52]. If we define the C phase connectivity as 1 for C nanofibers, then the C connectivity under different pyrolysis conditions for the SiOCs in this work can be obtained as shown in Fig. 9. It shows that polycrystalline C content can affect the electrical conductivity exponentially. At room temperature, the general relation is

$$y = 0.072 \exp\left(\frac{x}{4.360}\right) - 22.873. \quad (11)$$

**Fig. 9** Correlation of polycrystalline C content with **a** electrical conductivity and **b** connectivity



For the peak electrical conductivity at high temperatures, the general relation is

$$y = 0.004\exp\left(\frac{x}{3.303}\right) + 202.543, \quad (12)$$

where  $y$  is the conductivity,  $\text{S}\cdot\text{m}^{-1}$ ;  $x$  is the polycrystalline C content, wt%. The highest C connectivity sample has the highest electrical conductivity of  $705 \text{ S}\cdot\text{m}^{-1}$  even though the polycrystalline C content is only 38.76 wt%. Figure 9 also shows that at  $\sim 35\%$  C, the electrical conductivity and the C connectivity drastically increase. We believe that this is the connectivity threshold value for the studied SiOCs.

Comparing Fig. 9a and b, it should be noticed that the polymer precursor effect on the electrical conductivity is far less than the pyrolysis temperature effect for the studied systems. The fundamental reason is that the ordering of the polycrystalline C directly determines the conductivity and not the total amount of C. High pyrolysis temperatures can significantly increase the C ordering and connectivity.

There have been increasing needs for high thermal stability and high electrical conductivity materials. For the PMPS–15PHMS (at  $1300 \text{ }^\circ\text{C}$  pyrolysis temperature), this semi-conducting behavior with high thermal stability presents promising application potentials in high-temperature semi-conducting components. When the C ordering is too high (e.g.,  $1400 \text{ }^\circ\text{C}$ ), the corresponding oxidation vulnerability renders the system unsuitable for high-temperature use. Our future studies will focus on increasing the electrical conductivity without compromising the thermal stability of different SiOC systems.

## 4 Conclusions

SiOC ceramics derived from polysiloxane-based polymers with different side groups ( $\text{Si-H}$ ,  $\text{Si-CH}_3$ ,  $\text{Si-CH=CH}_2$ , and  $\text{Si-C}_6\text{H}_5$ ) have been investigated. The effects of C content on the phase evolution, thermal stability, and electrical conductivity of SiOC ceramics are examined. With an increase in the C content, the volumetric shrinkage increases, the ceramic yield decreases, and the bulk density also generally decreases in the wide temperature range of  $1200\text{--}1400 \text{ }^\circ\text{C}$ . Phase separation takes place at  $1000\text{--}1200 \text{ }^\circ\text{C}$  in the high-C content samples, much earlier than the low-C content samples. These SiOC composites demonstrate high electrical conductivity and thermal stability. In the Ar atmosphere, for the PMPS–15PHMS, the highest electrical conductivity is  $705.3 \text{ S}\cdot\text{m}^{-1}$  at  $403 \text{ }^\circ\text{C}$ , 52% higher than the results from our earlier work and more than 3.5 times of other results. Such high electrical conductivity is closely related to the high fraction of C with  $\text{sp}^2$  hybridization and increased ordering. A connectivity concept is introduced to explain the electrical

conductivity. The high-C SiOCs have promising application potentials in high-temperature semi-conducting components.

**Acknowledgements** We acknowledge the financial support from National Science Foundation under Grant number CMMI-1634325.

## References

1. C. Vakifahmetoglu, V. Presser, S.H. Yeon, P. Colombo, Y. Gogotsi, *Microporous Mesoporous Mat.* **144**(1–3), 105–112 (2011)
2. G.W. Liu, J. Kaspar, L.M. Reinold, M. Graczyk-Zajac, R. Riedel, *Electrochim. Acta* **106**, 101–108 (2013)
3. X. Liu, K. Xie, C.M. Zheng, J. Wang, *Acta. Phys. Sin-Ch. Ed.* **60**(11), 118202(1)–118202(6) (2011)
4. Y.W. Kim, J.H. Eom, C.B. Park, W. Zhai, Y. Guo, M. Balasubramanian, *J. Am. Ceram. Soc.* **93**(10), 3 (2010)
5. P.C.M. Fukushima, *J. Eur. Ceram. Soc.* **32**, 8 (2012)
6. H.R. Godini, H. Trivedi, A.G. de Villasante, O. Gorke, S. Jaso, U. Simon, A. Berthold, W. Witt, G. Wozny, *Chem. Eng. Res. Des.* **91**(12), 2671–2681 (2013)
7. R.I.S.M. Narisawa, K.I. Kita, H. Kado, H. Mabuchi, Y.W. Kim, *J. Appl. Polym. Sci.* **114**, 2600–2607 (2009)
8. K. Lu, D. Erb, M.Y. Liu, *J. Mater. Chem. C.* **4**(9), 1829–1837 (2016)
9. K. Wang, M. Günthner, G. Motz, R.K. Bordia, *J. Eur. Ceram. Soc.* **31**(15), 3011–3020 (2011)
10. A. Vomiero, S. Modena, G.D. Soraru, R. Raj, Y. Blum, G. Della Meas, *Nucl. Instrum. Meth. B.* **211**(3), 401–407 (2003)
11. J. Latournerie, P. Dempsey, D. Hourlier-Bahloul, J.P. Bonnet, *J. Am. Ceram. Soc.* **89**(5), 1485–1491 (2006)
12. K. Lu, *Mat. Sci. Eng. R.* **97**, 23–49 (2015)
13. D. Erb, K. Lu, *J. Eur. Ceram. Soc.* **37**(15), 4547–4557 (2017)
14. D. Hourlier, S. Venkatachalam, M.R. Ammar, Y. Blum, *J. Anal. Appl. Pyrol.* **123**, 296–306 (2017)
15. L. David, R. Bhandavat, U. Barrera, G. Singh, *Nat. Commun.* **7**, 10998 (2016)
16. P. Dibandjo, M. Graczyk-Zajac, R. Riedel, V.S. Pradeep, G.D. Soraru, *J. Eur. Ceram. Soc.* **32**(10), 2495–2503 (2012)
17. D. Ahn, R. Raj, *J. Power Sources* **195**(12), 3900–3906 (2010)
18. P.E. Sanchez-Jimenez, R. Raj, *J. Am. Ceram. Soc.* **93**(4), 1127–1135 (2010)
19. D. Ahn, R. Raj, *J. Power Sources* **196**(4), 2179–2186 (2011)
20. W.R. Schmidt, L.V. Interrante, R.H. Doremus, T.K. Trout, P.S. Marchetti, G.E. Maciel, *Chem. Mater.* **3**(2), 257–267 (1991)
21. G.D. Soraru, R. Pena-Alonso, M. Leoni, *Microporous Mesoporous Mat.* **172**, 125–130 (2013)
22. M. Halim, C. Hudaya, A.-Y. Kim, J.K. Lee, *J. Mater. Chem. A* **4**(7), 2651–2656 (2016)
23. Y.D. Blum, D.B. MacQueen, *Surf. Coat. Int. Pt. B-C* **84**(1), 27–33 (2001)
24. K. Lu, J.K. Li, *J. Eur. Ceram. Soc.* **36**(3), 411–422 (2016)
25. B.F. Sousa, I.V.P. Yoshida, J.L. Ferrari, M.A. Schiavon, *J. Mater. Sci.* **48**(5), 1911–1919 (2013)
26. M. Niu, H.J. Wang, J.W. Chen, L. Su, D. Wu, A. Navrotsky, *J. Am. Ceram. Soc.* **100**(8), 3693–3702 (2017)
27. R. Pena-Alonso, G.D. Soraru, R. Raj, *J. Am. Ceram. Soc.* **89**(8), 2473–2480 (2006)
28. H.J. Kleebe, C. Turquat, G.D. Soraru, *J. Am. Ceram. Soc.* **84**(5), 1073–1080 (2001)
29. E. Ionescu, B. Papendorf, H.J. Kleebe, F. Poli, K. Muller, R. Riedel, *J. Am. Ceram. Soc.* **93**(6), 1774–1782 (2010)

30. Y.D. Blum, D.B. MacQueen, H.J. Kleebe, J. Eur. Ceram. Soc. **25**(2–3), 143–149 (2005)
31. M. Mazo, A. Nistal, A. Caballero, F. Rubio, J. Rubio, J. Oteo, J. Eur. Ceram. Soc. **33**(6), 1195–1205 (2013)
32. K. Lu, D. Erb, M.Y. Liu, J. Mater. Sci. **51**(22), 10166–10177 (2016)
33. C.M. Brewer, D.R. Bujalski, V.E. Parent, K. Su, G.A. Zank, J. Sol-Gel, Sci. Techn. **14**(1), 49–68 (1999)
34. G.M. Renlund, S. Prochazka, R.H. Doremus, J. Mater. Res. **6**(12), 2723–2734 (1991)
35. G. Mera, A. Navrotsky, S. Sen, H.J. Kleebe, R. Riedel, J. Mater. Chem. A **1**(12), 3826–3836 (2013)
36. K.J. Kim, J.-H. Eom, Y.-W. Kim, W.-S. Seo, J. Eur. Ceram. Soc. **35**(5), 1355–1360 (2015)
37. J. Cordelair, P. Greil, J. Eur. Ceram. Soc. **20**(12), 1947–1957 (2000)
38. S. Martínez-Crespiera, E. Ionescu, H.-J. Kleebe, R. Riedel, J. Eur. Ceram. Soc. **31**(5), 913–919 (2011)
39. K. Wang, B. Ma, X. Li, Y. Wang, L. An, J. Am. Ceram. Soc. **97**(7), 2135–2138 (2014)
40. L. Toma, H.J. Kleebe, M.M. Muller, E. Janssen, R. Riedel, T. Melz, H. Hanselka, J. Am. Ceram. Soc. **95**(3), 1056–1061 (2012)
41. J. Kaspar, M. Graczyk-Zajac, S. Choudhury, R. Riedel, Electrochim. Acta **216**, 196–202 (2016)
42. S. Wu, R.B. Ladani, J. Zhang, E. Bafekrpour, K. Ghorbani, A.P. Mouritz, A.J. Kinloch, C.H. Wang, Carbon **94**, 607–618 (2015)
43. Z. Wang, Carbon **47**(13), 3050–3053 (2009)
44. J.M. Pan, J.F. Pan, X.N. Cheng, X.H. Yan, Q.B. Lu, C.H. Zhang, J. Eur. Ceram. Soc. **34**(2), 249–256 (2014)
45. C. Hintze, K. Morita, R. Riedel, E. Ionescu, G. Mera, J. Eur. Ceram. Soc. **36**(12), 2923–2930 (2016)
46. M. Wojcik-Bania, A. Lacz, A. Nyczyk-Malinowska, M. Hasik, Polymer **130**, 170–181 (2017)
47. M. Graczyk-Zajac, D. Vrankovic, P. Waleska, C. Hess, P.V. Sasikumar, S. Lauterbach, H.J. Kleebe, G.D. Soraru, J. Mater. Chem. A **6**(1), 93–103 (2018)
48. M.A. Mazo, A. Tamayo, A.C. Caballero, J. Rubio, J. Eur. Ceram. Soc. **37**(5), 2011–2020 (2017)
49. C.G. Pantano, A.K. Singh, H.X. Zhang, J. Sol-Gel, Sci. Techn. **14**(1), 7–25 (1999)
50. Y. Lim, J.H. Chu, D.H. Lee, S.-Y. Kwon, H. Shin, J. Alloy. Compd. **702**, 465–471 (2017)
51. S.K. Das, M.A.F. Afzal, S. Srivastava, S. Patil, A. Sharma, Carbon **108**, 135–145 (2016)
52. Z. Jun, J.-L. Xue, Y.-N. Zhang, L. Xiang, C. Tong, Trans. Nonferrous Met. Soc. China **25**(11), 3753–3759 (2015)

**Publisher's Note** Springer Nature remains neutral with regard to jurisdictional claims in published maps and institutional affiliations.